Journal of
Materials Chemistry A

Materials for energy and sustainability

Accepted Manuscript

This article can be cited before page numbers have been issued, to do this please use: J. Bejar, L. Alvarez-Contreras, J. Ledesma-García, N. Arjona and L. G. Arriaga, *J. Mater. Chem. A*, 2020, DOI: 10.1039/D0TA00874E.

ROYAL SOCIETY OF CHEMISTRY

rsc.li/materials-a

View Article Online
DOI: 10.1039/D0TA00874E

ARTICLE

An advanced three–dimensionally ordered macroporous $NiCo_2O_4$ spinel as bifunctional electrocatalyst for rechargeable Zn–Air batteries

Received 00th January 20xx,
Accepted 00th January 20xx

DOI: 10.1039/x0xx00000x

José Béjar[a], Lorena Álvarez-Contreras[b], Janet Ledesma-García[c], Noé Arjona[a]* and Luis Gerardo Arriaga[a]**

In this work, highly active $NiCo_2O_4$ spinels with three-dimensionally ordered macroporous (3DOM) structures were obtained using poly (methyl methacrylate) PMMA spheres as template, for which the high surface area of the 3DOM spinel, the presence of multi–valences of Co and Ni species and the high Ni content improve the activity for the oxygen reactions, presenting a current density value similar to that obtained for benchmarked Pt/C. Also, the spinel shows only 10 mV of overpotential compared with benchmarked IrO_2/C for oxygen evolution reaction (OER). The 3DOM spinel shows superior stability for both reactions, maintaining 80.5 (for ORR) and 100 % (for OER) of initial current after 10 h, respectively. This 3DOM spinel is used as an air electrode in a rechargeable Zn–air battery, enabling an open-circuit potential of 1.44 V, which is similar to that obtained for Pt/C (1.46 V), while also displaying a similar performance (109 *vs*. 101 mW cm^{-2}). Moreover, because of its excellent activity as a bifunctional electrocatalyst, the 3DOM spinel displays a superior charge–discharge capability after being operated for 21 h, while it provides successfully the energy requirements of a multi-sensor, which is operated for more than 2 h.

Introduction

Metal–air batteries are promising next-generation devices with higher performances to that presented by benchmarked Li-ion batteries. These electrochemical devices are powered by metal oxidation (using metals like Li, Zn, Mg and Na) and oxygen reduction[1]. Rechargeable Zn–air batteries (RZABs) can provide 5–fold higher energy density than conventional Li–ion batteries[2], and the lower cost of Zn metal make their fabrication attractive for commercialization purposes. The abundance of Zn metal in contrast with Li[3], and the political/social issues recently raised due to the concentration of this later metal in specific geographic places make urgent to overcome the limitations of RZABs components to obtain functional and durable energy storage devices.

RZABs are constituted by the Zn anode, an air electrode, separator/membrane, and electrolyte[4]. All of these components have their unique challenges to overcome as is described in several reviews[5–8]; however, the air electrode has the major contribution in the overpotential losses. The sluggish kinetics of oxygen reduction/evolution reactions (ORR/OER) plays a major role during the charge/discharge processes in a RZAB and thus, in the performance and durability. Thereby, the development of highly active and durable bifunctional materials is essential. Nowadays, plenty bifunctional electrocatalysts based on noble metals[9,10], mixtures of transition metal oxides (MTMOs)[11–14] and non-metallic materials[15–17] have been reported. Among them, MTMOs have displayed excellent electrocatalytic properties, and they have the advantage of being abundant, making them economically viable, as well as possessing an excellent stability and durability. In addition, MTMOs can be composed of a mix of different metals, and thus, tuneable electrocatalysts consisting of materials with high activities towards the ORR and OER can be easily synthesized to produce a synergistic effect[18]. One way to develop MTMOs sharing the crystalline network is through the spinel structure, which is described by the general formula AB_2X_4 (A = Li, Mn, Zn, Cd, Co, Cu, Ni, Fe, etc.; B = Al, Cr, Mn, Fe, Co, Ni, Ga, In, Mo, etc.; X = O, S, Se, Te, N, and others)[19]. In this manner, nanomaterials with a spinel structure based on nickel, cobalt, and manganese have been extensively reported as bifunctional electrocatalysts for metal-air batteries[20–22], for which the $NiCo_2O_4$ spinel has displayed high functionality as air electrode for RZABs due to its intrinsic high activity, corrosion resistance, and easy availability[19].

The electrocatalytic activity of $NiCo_2O_4$ spinels can be modulated by tuning the crystallite size, Ni:Co atomic rate, particle size and shape, and electrical conductivity, as well as controlling metal valences, creating defects, and selecting the proper conductive support, causing shifts in the atomic arrangement and electronic properties[19]. In terms of atomic arrangement, different $NiCo_2O_4$ and Co_3O_4 morphologies, as nanoparticles[21–23], nanocubes[24–26], nanowires[27–29], and nanoneedles[30,31], among others, have been developed to improve

[a] Centro de Investigación y Desarrollo Tecnológico en Electroquímica S. C., Querétaro, C. P. 76703, México
[b] Centro de Investigación en Materiales Avanzados S. C., Complejo Industrial Chihuahua, Chihuahua, C. P. 31136, México
[c] Facultad de Ingeniería, División de Investigación y Posgrado, Universidad Autónoma de Querétaro, Querétaro, C. P. 76010, México
Electronic Supplementary Information (ESI) available: [details of any supplementary information available should be included here]. See DOI: 10.1039/x0xx00000x

View Article Online
DOI: 10.1039/D0TA00874E

the specific surface area (SSA) and thus, the electrocatalytic activity. An uncommon method to improve the SSA consist of developing materials employing polymer templates that can help to obtain a defined morphology[32]. Among these nanostructures, three–dimensionally ordered macroporous morphologies (3DOMs) have allowed novel electrocatalysts to emerge. These electrocatalysts are promising because the periodic pore arrangement enables a high SSA as well as a better interaction between active sites and reactants.[33,34]

Most of the reported 3DOM materials are based on carbon or transition metals and have been prepared specifically for soot combustion[35–39], where 3DOM materials with above 50 nm average pore diameters[36] allow soot particles (>25 nm) to enter into the inner pores to react. Regarding oxygen reactions, few works have dealt with 3DOM materials as bifunctional electrocatalysts, with one of them based on 3DOM perovskites[40] and the other based on a 3DOM Co_3O_4 spinel.[41] To our knowledge, there are no reports concerning bimetallic spinels in a 3DOM morphology for the oxygen reduction and evolution reactions. Moreover, in most of the mentioned works, the 3DOM structures were constructed using a polymer template with particle sizes larger than 300 nm, because their application in soot combustion; however, for oxygen reactions, particle sizes smaller than 300 nm can be beneficial to attain higher surface areas.

In this work, we report for the first time, the synthesis of three spinels materials Co_3O_4, $Ni_{0.5}Co_{2.5}O_4$ and $NiCo_2O_4$ with a 3DOM structure. These materials are evaluated as bifunctional electrocatalysts for the oxygen reduction and evolution reactions using benchmarked Pt/C and IrO_2/C, and their mixture as reference electrocatalysts. The effect of Ni incorporation in the cobalt oxide structure to form bimetallic spinels ($Ni_{0.5}Co_{2.5}O_4$ and $NiCo_2O_4$) is studied in terms of changes in surface area, electrical conductivity and electrocatalytic activity. Moreover, the activity of 3DOM $NiCo_2O_4$ is tested in a Zn–air battery, where the higher performance achieved by this material, in contrast with that of Pt/C and IrO_2/C, is attributed to a greater activity and stability.

EXPERIMENTAL

Synthesis of 3DOM electrocatalysts

The 3DOM materials were synthesized using a poly (methyl methacrylate) (PMMA) colloidal crystal template (CCT). The detailed procedure for the polymerization and CCT assembly is described in the supplementary information (SI, Fig. S1). According to the followed methodology, PMMA microspheres with a diameter close to 160 nm were synthesized via emulsion polymerization [42,43](Fig. S2). The 3DOM spinels were prepared by making modifications to a previously reported CCT method.[44] Briefly, 1 g citric acid (Sigma–Aldrich, ≥99.5 %), as complexing agent, was added to 20 mL methanol (Sigma–Aldrich, ≥99.9 %) and stirred for 1 h to obtain a uniform precursor solution. Then, suitable amounts of $Co(NO_3)_2 \cdot 6H_2O$ (Sigma–Aldrich, ≥98.0 %) and $Ni(NO_3)_2 \cdot 6H_2O$ (Sigma–Aldrich, ≥97.0 %) metal nitrate precursors were dissolved with stirring at 35 °C for 4 h, keeping 1 mol L^{-1} total metal concentration.

The impregnation of the PMMA hard template was carried out under vacuum. Similar methodology was followed for the three spinels (Co_3O_4, $Ni_{0.5}Co_{2.5}O_4$ and $NiCo_2O_4$). For this purpose, a piece of CCT (Fig. S1, ∼2 g in weight) was placed inside of a Buchner funnel in a vacuum filtration system. Then, 6 layers of 3 ml precursor solution (each one) were deposited, applying vacuum for 5 min between each layer. Finally, the material was submitted to vacuum for 2 h to eliminate excesses. The obtained precursor/template mixture was dried in air at 50 °C for 24 h. Then, the sample was calcined in a tube furnace to remove the PMMA hard template. The thermal treatment process was carried out in two steps: (1) the dried solid was calcined under 90 mL min^{-1} N_2 flow and 1 °C min^{-1} of temperature rate until 310 °C, and this temperature was maintained for 3 h. (2) The treated solid was then kept at 310 °C under 90 mL min^{-1} air flow for 1 h, and then, the temperature was increased until 550°C at 1 °C min^{-1} under air atmosphere and held for 4 h.

Physicochemical characterization

PMMA CCT was characterized by scanning electron microscopy (SEM) using a field–emission scanning electron microscope (JEOL JSM–7401F) to confirm the formation of the CCT assembly. The structure of the 3DOM materials was also analysed by SEM using the JEOL JSM-7401F microscope, while elemental mapping was performed via energy–dispersive X–ray spectroscopy (EDS) using a Bruker EDX detector coupled to a Hitachi H7700 apparatus. Further morphological analysis was performed by transmission electron microscopy (TEM, Hitachi H7700), where the particle sizes and *d*–spacings were calculated using the ImageJ® software.[45] In addition, selected area electron diffraction (SAED) patterns obtained using the Hitachi TEM apparatus were also analysed by the ImageJ® software to determine the crystalline planes in the spinels. BET surface area analysis was performed using N_2 adsorption/desorption isotherms employing a Quantachrome® S–BET Autosorb iQ2, and the Barret–Joyner–Halenda (BJH) method was used to report surface areas. These materials were further characterized by X–ray diffraction (XRD) and X–ray photoelectron spectroscopy (XPS) using a Bruker D8 Advance diffractometer operated at 30 kV and 30 mA and a Thermo Scientific Escalab 250 Xi XPS apparatus, respectively. The photoelectrons were generated with a monochromatic Al Ka (1486.68 eV) X–ray source. Survey spectra of the samples were collected over 1100 eV range at 1 eV per step, 100 ms and a 150 eV pass energy. High–resolution spectra were collected for the chemical species of interest at 0.1 eV per step and 20 eV pass energy. All measurements were done under ultra–high vacuum conditions (10^{-10} torr). The deconvolved XPS spectra were normalized using the O 1s peak, which was adjusted using the reported value (531.0 eV).[46]

Electrocatalytic evaluation

The electrochemical and electrocatalytic characterization of materials was performed using a BioLogic® Potentiostat/

Galvanostat. For this purpose, a three–electrode glass–jacketed electrochemical cell was used. The electrochemical configuration consisted of using Hg/HgO 1M KOH electrode and a graphite rod as the reference and counter electrode, respectively. Rotating disk electrode with glassy carbon tips (Pine®, 0.07 cm^2) was used as the working electrode for the ORR and with gold tips for the OER (the influence of gold was discarded through an electrochemical test determining the number of catalyst layers needed to overlap its signal Fig. S3). Additionally, 0.1 M KOH was employed as the electrolyte for all experiments. 3DOM spinels and benchmarked electrocatalysts (Pt/C 20 wt.%, IrO_2/C 20 wt.% from E–TEK, and their mixture in a 1:1 mass ratio) were deposited onto working electrodes through catalytic inks. The ink was prepared using isopropyl alcohol as dispersant and Nafion® 117 (Sigma–Aldrich, 5 wt.% in isopropyl alcohol) as the binder. Two kinds of catalytic inks were prepared: one for 3DOM spinels, where 6 mg catalyst, 270 µL isopropyl alcohol and 45 µL Nafion were mixed and sonicated for 30 min, and then, 5 layers of 1 µL solution were transferred to the electrode, maintaining 0.27 mg cm^{-2} of total catalyst mass. Catalytic inks for Pt/C and IrO_2/C were prepared by the above procedure using catalyst loadings close to0.135 mg cm^{-2} of total catalyst mass (only 2–fold lower catalyst mass to that used for 3DOM materials).

Cyclic voltammetry was performed to obtain the electrochemical profiles in alkaline media. The cyclic voltammograms were recorded in a potential range between 0.04 and 1.59 V *vs*. RHE (reversible hydrogen electrode) for spinels-based materials and between 0 and 1.3 V *vs*. RHE for Pt/C. The scan rate used in the tests was 20 mV s^{-1}, and 50 cycles were recorded under an inert atmosphere using nitrogen gas (Praxair, 5.0 for research purposes). The electrocatalytic activity toward ORR and OER was evaluated using the rotating disk electrode (RDE) technique by varying the rotatory speed. For the ORR, linear sweep voltammograms (LSVs) were acquired using a potential range from 0.14 to 1.04 V *vs*. RHE at a scan rate of 5 mV s^{-1} (For 3DOM spinels and IrO_2/C) and a range from 0.26 to 1.14 V *vs*. RHE for Pt/C at the same scan rate. In addition, the experiments for the OER were performed in a nitrogen–rich solution using 1600 rpm as the rotatory speed for a potential window from 0.94 to 1.94 V *vs*. RHE at 5 mV s^{-1}. The stability tests were performed by chronoamperometry technique. The ORR stability was determined at the half–wave potential of each material while maintaining a rotation speed of 1600 rpm and constant oxygen bubbling for 10 h. Meanwhile, the OER stability was evaluated at the potential found at 10 mA cm^{-2} for each material while maintaining a rotation speed of 1600 rpm and constant nitrogen bubbling for 10 h. Additionally, electrochemical impedance spectroscopy (EIS) was performed to analyse the electrical properties of the 3DOM materials, specifically the resistance to charge transfer (Rct). The measurements were taken at 0.82 V *vs*. RHE with the frequency ranging from 100 kHz to 0.01 Hz.

Zn–Air battery device

The Zn–air battery was constructed using two PMMA plates and a polydimethylsiloxane (PDMS) separator / electrolyte chamber (Fig. 8c, inset). The battery dimensions were 35×25×13 mm in length, width and depth respectively, while the upper PMMA plate (5 mm in depth) had an air window of 15×3 mm length and width (patterned using CNC machining). The PDMS film used as the separator / chamber had the same shape and dimensions as those of the PMMA plates; however, the thickness of this film was 3 mm, and the chamber is 15×6 mm (length and width, which is depicted as a green film in Fig. 8c, inset). The electrode dimensions were patterned into the PMMA plates to serve as guides when placing the electrodes. The anode consisted in a polished high–purity Zn foil (25×3 mm length and width, and 0.5 mm in depth; Belong Store® China) with 15 mm effective length, while 0.2 M $ZnCl_2$ (Granular, J. T. Baker) dissolved in 4 M KOH (87 %, Sigma–Aldrich) was used as the electrolyte. SIGRACET® 39B slides (25×3 mm length and width, and 0.4 mm in depth) impregnated with the catalytic ink were used as the air electrodes. The catalyst loading was 1 mg cm^{-2} for Pt/C, IrO_2/C and their mixture, and 2 mg cm^{-2} for the $NiCo_2O_4$. A BioLogic® Potentiostat/Galvanostat was used to analyse the battery charge/ discharge performance and stability. The stability determination consisted of an accelerated charge and discharge test performed at 10 mA cm^{-2} during 150 cycles with a time of 500 seconds per cycle. Moreover, the current was normalized to the Zn geometric area (0.45 cm^2).

RESULTS AND DISCUSSION

Physicochemical results

XRD patterns for Co_3O_4 (Fig. 1a-I) and $Ni_{0.5}Co_{2.5}O_4$ (Fig. 1a-II) present nine characteristic diffraction peaks, where according to their positions (Table S1), they can be indexed to the (111), (220), (311), (222), (400), (422), (511), (440) and (533) planes of the cubic structure of Co_3O_4 and $NiCo_2O_4$ spinels (PDFS number 03-065-3103 and 00-020-0781, respectively).[47] $NiCo_2O_4$ material (Fig. 1a-III) presented shifts in diffraction peaks with respect to those of Co_3O_4 (Table S1), suggesting a substitutional incorporation of Ni into the Co_3O_4 structure. The absence of additional peaks also suggested that there was no secondary phase (or impurity) in any of these materials. In addition, the elemental composition analyzed by EDS (Table S2) and XPS (Table S3) together with the theoretical and experimental positions and *d*–spacings (Table S1) corroborated the formation of these spinels. Moreover, the crystallite sizes were determined by the Debye–Scherrer equation.[48] The calculated crystallite sizes were 12.3, 9.4 and 9.3 nm for Co_3O_4, $Ni_{0.5}Co_{2.5}O_4$ and $NiCo_2O_4$, respectively.

BET surface areas were obtained from nitrogen ads/desorption isotherms (Fig. 1b). The ads/desorption behaviour indicated a mixture of types 2 and 4 isotherms and a type H3 hysteresis loop. The latter description reveals that the isotherms did not show any limiting adsorption at high P/Po in the range of 0.7–1, which is characteristic of mesoporous materials[41,49,50]. BET surface areas of 39.6, 46.4 and 46.8 m^2 g^{-1} were obtained for Co_3O_4 (Fig. 1b-I), $Ni_{0.5}Co_{2.5}O_4$ (Fig. 1b-II) and

$NiCo_2O_4$ (Fig. 1b-III), respectively, with pore volumes of 0.286, 0.289 and 0.286 $m^3\ g^{-1}$. These results were attributed to the mesopores observed in the results of the pore size distributions (Fig. 1b insets). Concerning the effect of the nickel addition to the cobalt spinel, is possible to conclude that nickel had a positive effect because it increasing the surface area by 8 $m^2\ g^{-1}$ (approximately 20%), while a non–notable difference was observed for the amounts of nickel in the $Ni_{0.5}Co_{2.5}O_4$ and $NiCo_2O_4$ materials. Finally, the use of the template with spheres approximately 160 nm in size benefited the surface area, obtaining values higher than similar materials with spheres of 250 nm and above.[40,41]

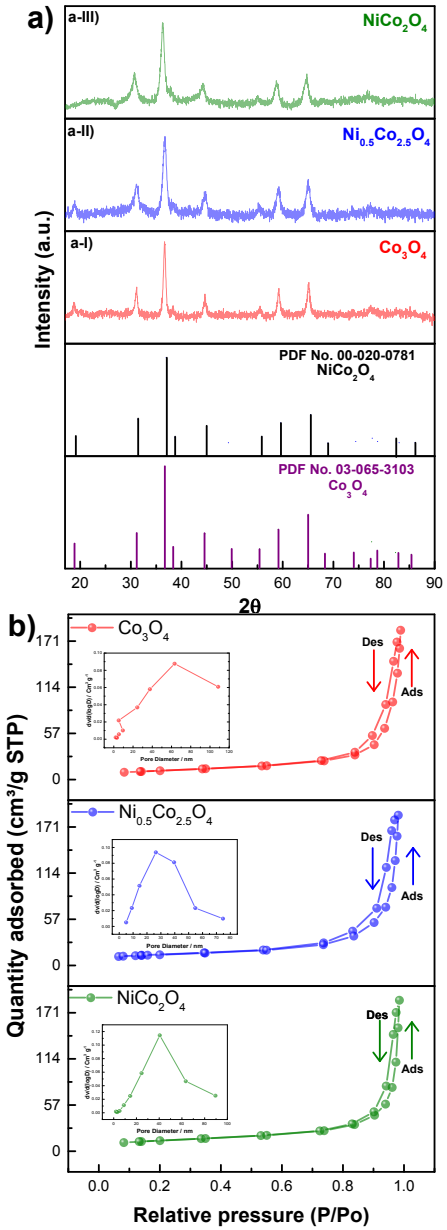

Figure 1. a) XRD patterns of the 3DOM electrocatalysts Co_3O_4 (a-I), $Ni_{0.5}Co_{2.5}O_4$ (a-II) and $NiCo_2O_4$ (a-III) and b) Nitrogen adsorption-desorption isotherms and pore-size distribution plots (inset) for Co_3O_4 (b-I), $Ni_{0.5}Co_{2.5}O_4$ (b-II) and $NiCo_2O_4$ (b-III).

The morphology and microstructure of the 3DOM materials were analysed by SEM and TEM. SEM micrographics demonstrate well–defined periodically macroporous structure and interconnected network of these materials (Figs. 2a, 2c and 2e), being the bimetallic spinels the materials with better periodicity (Figs. 2c, and 2d). Two main pore sizes were found, regardless of the material; the first type was large macropores, which formed upon the removal of the PMMA spheres, and they are called "skeletons". The diameter of these skeletons was found to be close to 130-140 nm (Figs. 2b, 2d, and 2f). The second type of pores comprised the so-called "window pores", being these pores generated by contact points between PMMA spheres. For this case, window pore sizes close to 50 nm were found. Additionally, the wall thickness was found to be 16 nm. The obtained skeleton sizes were lower than the diameter of the PMMA microspheres (160 nm), and this size reduction was attributed to the shrinkage of PMMA microspheres during the calcination of the metal nitrates, because PMMA may experience a contraction at glass transition temperature. Previous works have also observed a substantial shrinkage when preparing 3DOM materials.[44,51,52]

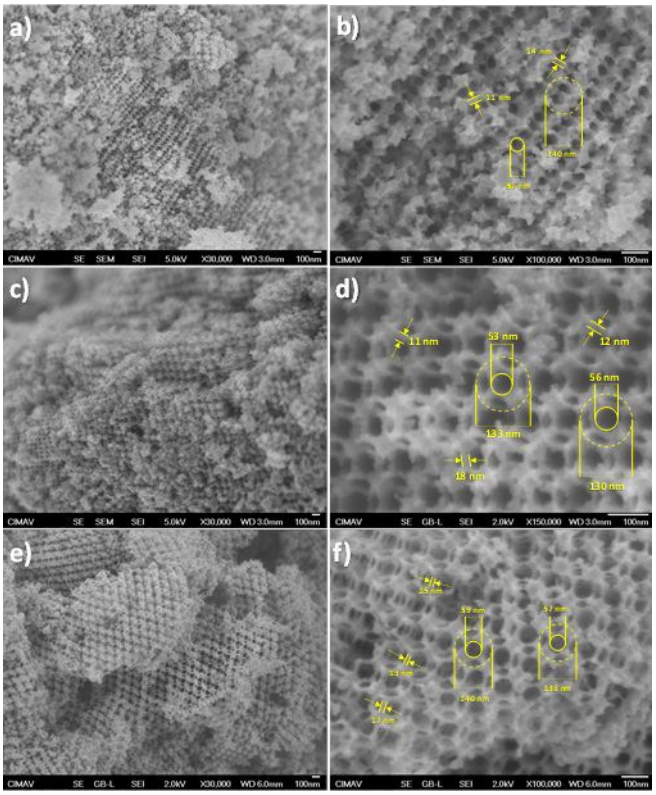

Figure 2. SEM images at two different magnifications for a & b) Co_3O_4; c & d) $Ni_{0.5}Co_{2.5}O_4$; and e & f) $NiCo_2O_4$. Figs. a, c and e display the 3DOM periodicity and Figs. b, d and f the open window sizes and wall thickness.

TEM micrographs of Co_3O_4 (Fig. 3a), $Ni_{0.5}Co_{2.5}O_4$ (Fig. 3b) and $NiCo_2O_4$ (Fig. 3c) corroborated the existence of 3DOM structures. Sizes close to the 50 nm of the window pores can be observed in Figs. 3a–I, 3b–I, and 3c–I. In addition, the small particle size of the spinels can be observed in Figs. 3a–II, 3b–II, and 3c–II. Histograms of the particle distributions are insets in these figures; as shown, the Co_3O_4 particles displayed a size of 11.9 ± 0.9 nm, while the $Ni_{0.5}Co_{2.5}O_4$ and $NiCo_2O_4$ particles had sizes of 8.6 ± 0.9 nm and 9.6 ± 1.0 nm, respectively.

View Article Online
DOI: 10.1039/D0TA00874E

ARTICLE

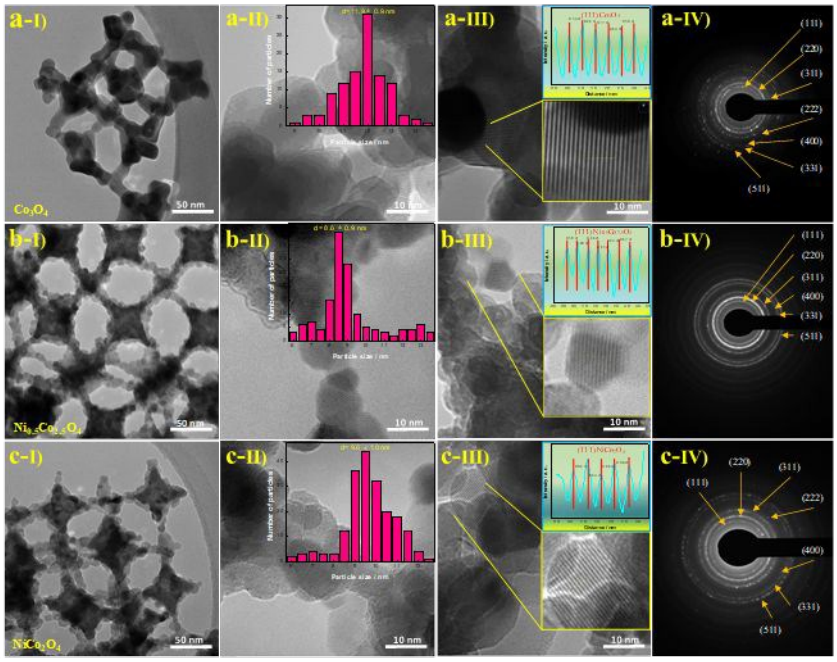

Figure 3. TEM images and SAED patterns of aI-IV) Co_3O_4, bI-IV) $Ni_{0.5}Co_{2.5}O_4$ and cI-IV) $NiCo_2O_4$.

These particle sizes agreed with the crystallite sizes. Furthermore, TEM micrographs at higher magnifications were taken to analyze the lattice fringes (Figs. 3a–III, 3b–III, and 3c–III). Magnifications of selected areas are shown in the insets of these figures to reveal the lattice fringes used for calculating *d*–spacings with the ImageJ® software. The *d*–spacing patterns, as a function of distance between lattice fringes (yellow line), indicated that the obtained *d*–spacings were enclosed to that of the (111) plane. Moreover, the ring distances in the SAED patterns (Figs. 3a–IV to 3c–IV) corroborated the formation of spinel structures because the indexed crystalline planes agreed with those reported in the above mentioned XRD results (Table S1).

EDS mappings of the bimetallic spinels (Figs. 4a and 4b for $Ni_{0.5}Co_{2.5}O_4$ and $NiCo_2O_4$, respectively) confirmed the homogeneous distributions of Ni and Co in the material. Meanwhile, the elemental analysis showed that the stoichiometries of these materials were close to the calculated compositions (Table S2). In addition, the porous structure was highlighted by the elemental distributions since the elements only appeared on the skeletons. However, it should be noted that although the materials were dispersed by sonication for the EDS analysis, both maintained their well–connected walls, which was important for the further electrochemical characterization/ evaluation. It was observed in the SEM and TEM images that hierarchically ordered pores resulted in a honeycomb-like mesoporous structure, where the open structure could provide a high surface area exposing more active sites needed for the oxygen electrochemical reactions (ORR / OER) as was observed by BET results.

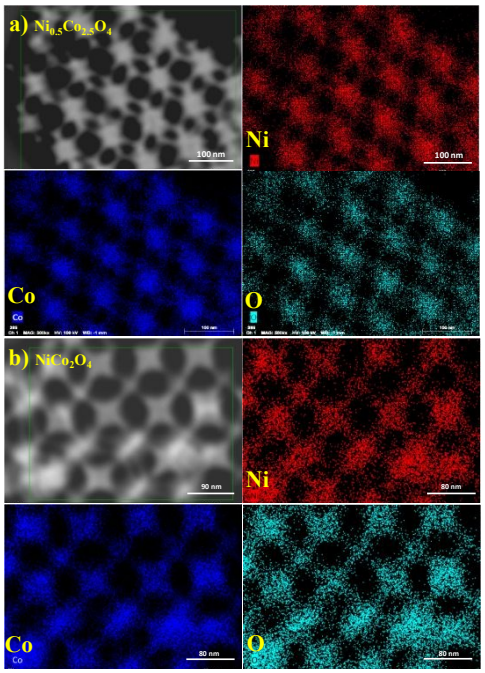

Figure 4. EDS elemental mapping for a) $Ni_{0.5}Co_{2.5}O_4$ and b) $NiCo_2O_4$.

XPS was used to analyze the metal species in surface layers of the catalysts, composition (Table S3) and the changes in the structure of Co_3O_4 in the presence of nickel (Fig. 5). Figures 5a to 5c show the high–resolution XPS spectra of the Co 2p core level. Co_3O_4 (Fig. 5a) displayed peaks at 779.74 eV and 795 eV that were attributed to Co^{3+}, while the peaks at 781.19 eV and 796.84 eV were assigned to Co^{2+}.[53] $Ni_{0.5}Co_{2.5}O_4$ (Fig. 5b) presented the same peaks at 779.58 eV and 794.83 eV for Co^{3+} and at 781.12 eV and 796.75 eV for Co^{2+}, while $NiCo_2O_4$ (Fig. 5c) presented the peaks related to Co^{3+} at 779.59 eV and 794.91 eV and those related to Co^{2+} at 781.14 eV and 797.02 eV. High–resolution XPS spectra of the Ni 2p core level are displayed in Figs. 5d and 5e, where both spectra showed two spin–orbit doublets corresponding to Ni^{2+} and Ni^{3+} species. $Ni_{0.5}Co_{2.5}O_4$ (Fig. 5d) presented peaks assigned to Ni^{2+} at 854.39 eV and 871.76 eV and to Ni^{3+} species at 856.06 eV and 873.41 eV. In the case of $NiCo_2O_4$ (Fig. 5e), similar peaks were observed at 854.12 eV and 873.33 eV for Ni^{2+} and at 855.95 eV and 873.53 eV for Ni^{3+} species.[54–56] To understand the structural changes generated by the addition of nickel, it was necessary the introduction of a more suitable format for a spinel, given by $A_{1-x}B_x(A_xB_{2-x})O_4$, from which three assumptions can be made: x=0 corresponds to a normal spinel (Co_3O_4), x=1 is attributed to an inverse spinel, and 0<x<1 refers to a complex spinel.[19] For example, when 0.5 nickel is added, the material is in the regime of a complex spinel; on the other hand, when x=1 is reached, it should be an inverse spinel. However, from XPS results it can observe that $NiCo_2O_4$ exhibited the four species with a clear decrease in Co^{2+}, and from previous reports, the conclusion is that a more exact formula for $NiCo_2O_4$ is $Co^{2+}{}_{1-x}Co^{3+}{}_x[Co^{3+}Ni_{2+x}Ni^{3+}{}_{1-x}]O_4$ ($0 \leq x \leq 1$)[53] (cations within the square bracket are in the octahedral sites, and cations outside the brackets occupy the tetrahedral sites).

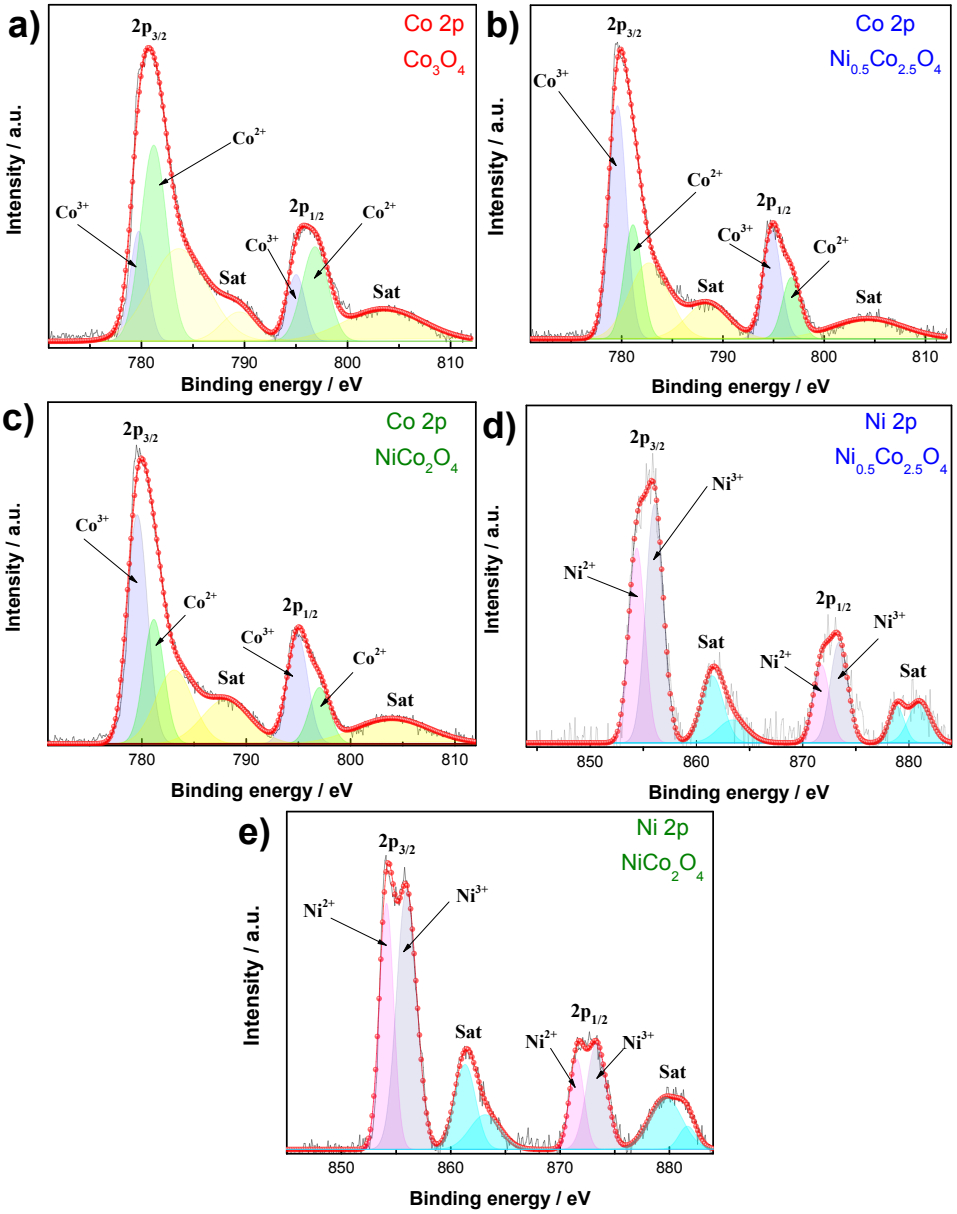

Figure 5. High-resolution XPS spectra of Co 2p a) Co_3O_4, b) $Ni_{0.5}Co_{2.5}O_4$, and c) $NiCo_2O_4$ and Ni 2p spectra for d) $Ni_{0.5}Co_{2.5}O_4$ and e) $NiCo_2O_4$

View Article Online
DOI: 10.1039/D0TA00874E

ARTICLE

Electrochemical evaluation

The electrochemical profile of Co_3O_4 (Fig. S4, red line) displayed three anodic peaks at 1.05 (labelled as I), 1.28 (II) and 1.54 V(III) *vs.* RHE. According to the literature, these peaks could be attributed to the formation of several cobalt species such as $Co(OH)_2$, Co_3O_4, CoOOH and CoO_2, which are stable in alkaline solutions. During the backward scan, two peaks at 1.47 (IV) and 1.20 V *vs.* RHE(V) are observed and attributed to the reduction of the as-formed oxide/hydroxides species. This behavior could be related to the redox reaction between Co^{2+}/Co^{3+} and Co^{3+}/Co^{4+} species,[57,58] while peak VI is associated with the ORR. The electrochemical profiles of $Ni_{0.5}Co_{2.5}O_4$ (blue line) and $NiCo_2O_4$ (green line) were similar, displaying two pairs of oxidation/reduction peaks labelled as peaks I to IV. Peaks I and II generated during the cathodic scan correspond to the oxidation of Co and Ni species. On the other hand, the peak generated during the anodic sweep (III) is attributed to the reduction of the species generated during the cathodic sweep. Finally, peak IV is associated with oxygen reduction.[59–61]

ORR/OER in half-cell. Concerning the electrocatalytic evaluation of synthesized materials toward oxygen reduction, Fig. 6a displays the linear sweep voltammetry curves at different rotatory speeds of $NiCo_2O_4$, as representative electrocatalytic material, while the electrocatalytic responses of the Co_3O_4 and $Ni_{0.5}Co_{2.5}O_4$ 3DOM materials and benchmarked Pt/C and IrO_2/C are presented in Fig. S5. These five materials displayed increases in current density with the rotatory speed, reaching stationary currents during each speed. These materials presented differences in onset potentials (E_{onset}) and current densities; however, prior to this discussion, the number of transferred electrons was obtained for determining the material effect on the oxygen reduction pathway. For this purpose, Koutecky–Levich plots were obtained at three potentials and are shown as insets in Figs. 6a and S5.

Koutecky–Levich plots displayed in Figs. 6a and S5 also include the theoretical descriptions of the $2e^-$ and $4e^-$ pathways. $NiCo_2O_4$ electrocatalyst (Fig. 6a, inset) clearly displayed a $4e^-$ pathway, presenting an electron transfer number (n) of 3.9 e^-. In the case of the other 3DOM materials, Co_3O_4 yielded n=3.6 e^-, and $Ni_{0.5}Co_{2.5}O_4$ showed n=3.7 e^-. Pt/C exhibited the typical 4 e^- pathway, with an electron transfer number closed to $4e^-$; however, IrO_2/C had a tendency for both pathways evidenced by a n=3.2 e^-, suggesting that the formation of hydrogen peroxide from the $2e^-$ pathway could compromise the activity and stability of this catalyst during the ORR. In fact, the comparison of the activity performed at 1600 rpm as a reference (Fig. 6b), indicated that the lowest performance was achieved by IrO_2/C, which could be attributed to the followed oxygen reduction pathway. This comparison also showed that the bimetallic 3DOM materials had excellent performance towards the ORR, reaching current densities like that obtained when Pt/C (e.g., 5.11 *vs.* 5.25 mA cm^{-2}) is used (Table S4). In terms of onset potential (E_{onset}), the $NiCo_2O_4$ electrocatalyst had the most similar value to that obtained with Pt/C (η= 80 mV) as catalyst, while the lowest current density and E_{onset} were found for IrO_2/C (Fig. 6b, Table S3). In addition, is worth mentioning that reports have described MTMOs as bifunctional catalysts that presented E_{onset} and half–wave potential ($E_{1/2}$) values closed to those obtained by using Pt/C. Nonetheless, these values were achieved using specific supports, such as graphene or carbon nanotubes. In this work, Vulcan carbon was used as the support, and despite this, the herein presented 3DOM materials performed similar electrocatalytic activities to those of the already reported materials. Moreover, the 3DOM materials also presented activities superior to those of other materials that were evaluated using a Vulcan carbon or carbon black support (Table S5). Concerning the Tafel plots (Fig. 6c), the $NiCo_2O_4$ spinel showed a similar behavior to that obtained when Pt/C was used as catalyst, presenting values of 97.3 and 96.6 mV Dec^{-1}, which indicated similar electrode kinetics. Moreover, the $NiCo_2O_4$ spinel yielded lower values than that obtained by using Co_3O_4 and $Ni_{0.5}Co_{2.5}O_4$ materials. This improvement could be attributed to the effect of the Ni^{3+} species in the $NiCo_2O_4$ spinel, enabling a higher electronic conductivity and thus, a lower resistance to charge transfer (Rct). Rct values were measured by electrochemical impedance spectroscopy for 3DOM materials at 0.82 V during the ORR (Fig. S6), obtaining values of 2743 (Co_3O_4), 931 ($Ni_{0.5}Co_{2.5}O_4$) and 413 ($NiCo_2O_4$) Ω cm^2. The R_{ct} value obtained by $NiCo_2O_4$ was 4.8 and 2.2 times lower to that obtained for Co_3O_4 and $Ni_{0.5}Co_{2.5}O_4$, respectively. As can be observed, the higher Ni content in the $NiCo_2O_4$ spinel enabled a lower R_{ct}, which could be contributing to the activity towards the ORR. Finally, the stability of these materials was tested by chronoamperometric tests for 10 h in the presence of constant O_2 atmosphere (Fig. 6d). 3DOM materials showed a superior stability compared with that obtained when was used Pt/C, maintaining 80.5 % ($NiCo_2O_4$), 76.8 % ($Ni_{0.5}Co_{2.5}O_4$) and 69.6 % (Co_3O_4) of their initial current, while Pt/C only retained 50.3 %. The improved stability of the 3DOM spinels could be related to the 3DOM structure with well–defined ordered pores and low crystallite sizes.

View Article Online
DOI: 10.1039/D0TA00874E

ARTICLE

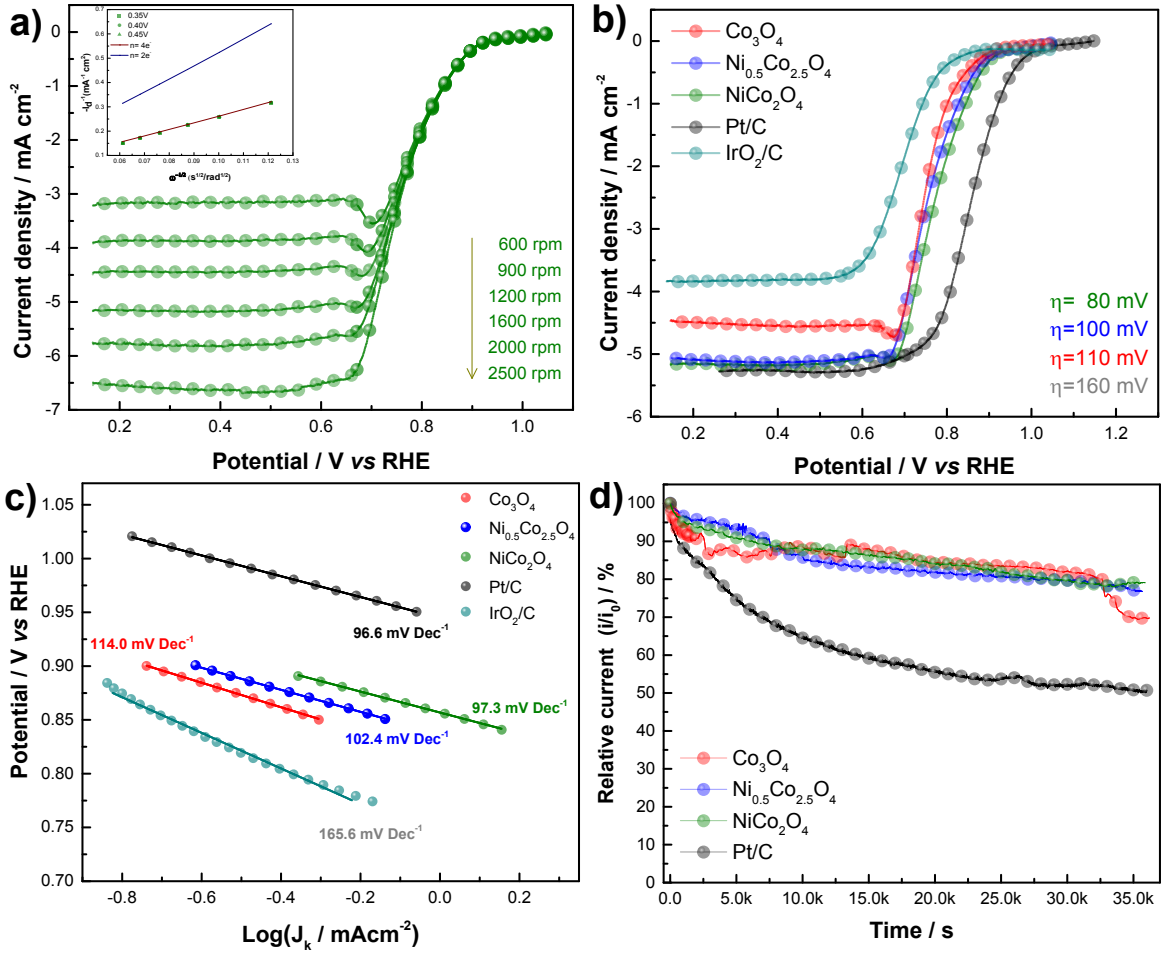

Figure 6. a) Linear voltammograms of $NiCo_2O_4$ at different rotation speeds and the K-L plot (inset). b) Linear voltammograms of the 3DOM spinels, Pt/C and IrO_2/C for the ORR at 1600 rpm rotating speed. c) Tafel plots determined from the corresponding linear voltammetry data. d) Chronoamperometric curves for the ORR stability under O_2-saturated 0.1 M KOH for the 3DOM spinels and Pt/C.

Concerning the oxygen evolution reaction OER, the LSV curves (Fig. 7a) showed that the activity was greatly influenced by nature/composition of the electrocatalyst. As expected, IrO_2/C, as the best catalyst for the reaction, which required a low potential to achieve 10 mA cm^{-2} (1.63 V vs. RHE). However, $NiCo_2O_4$ 3DOM spinel displayed a similar activity, needing only 10 mV more than that overpotential performed by IrO_2/C to achieve 10 mA cm^{-2}. The bimetallic 3DOM spinel with a low Ni content ($Ni_{0.5}Co_{2.5}O_4$) utilized 1.71 V to achieve this current, while the monometallic 3DOM spinel (Co_3O_4) and Pt/C required 1.75 V and 1.82 V, respectively. Then, the activity trend for the OER assumed: $IrO_2/C \geq NiCo_2O_4 > Ni_{0.5}Co_{2.5}O_4 > Co_3O_4 > Pt/C$. The Tafel plots (Fig. 7b) were obtained to explain the activity changes. In this way, the Tafel slope for the $NiCo_2O_4$ 3DOM spinel was less (65 mV Dec^{-1}) than that for the rest of the materials (Fig. 7b, inset values), indicating a faster reaction kinetics. In addition, a higher activity was accompanied by the presence of Co^{3+} and Ni^{3+} species, because these species promote the adsorption of OH^- ions, generating species such as CoOOH and NiOOH that are responsible for the OER. [62–64]

The stability tests (Fig. 7c) were performed at the potential required to reach 10 mA cm^{-2} each material. The results showed that $NiCo_2O_4$ proved to be the most stable material for the OER, maintaining 100% of initial current. IrO_2/C catalyst, despite being considered as one of the most active catalysts, only maintained 30.9% of initial current. $Ni_{0.5}Co_{2.5}O_4$ catalyst kept 90% of initial current after 10 h, while Co_3O_4 kept 32 %. The higher stability of $NiCo_2O_4$ could be related not only the morphology that allowed a better mass transport, also to the presence of Ni^{3+} and Ni^{2+} species, which has been reported to improve the conductivity and corrosion resistance[64]. ORR and OER thermodynamically occurs at 1.23 V vs. RHE. However,

View Article Online
DOI: 10.1039/D0TA00874E

ARTICLE

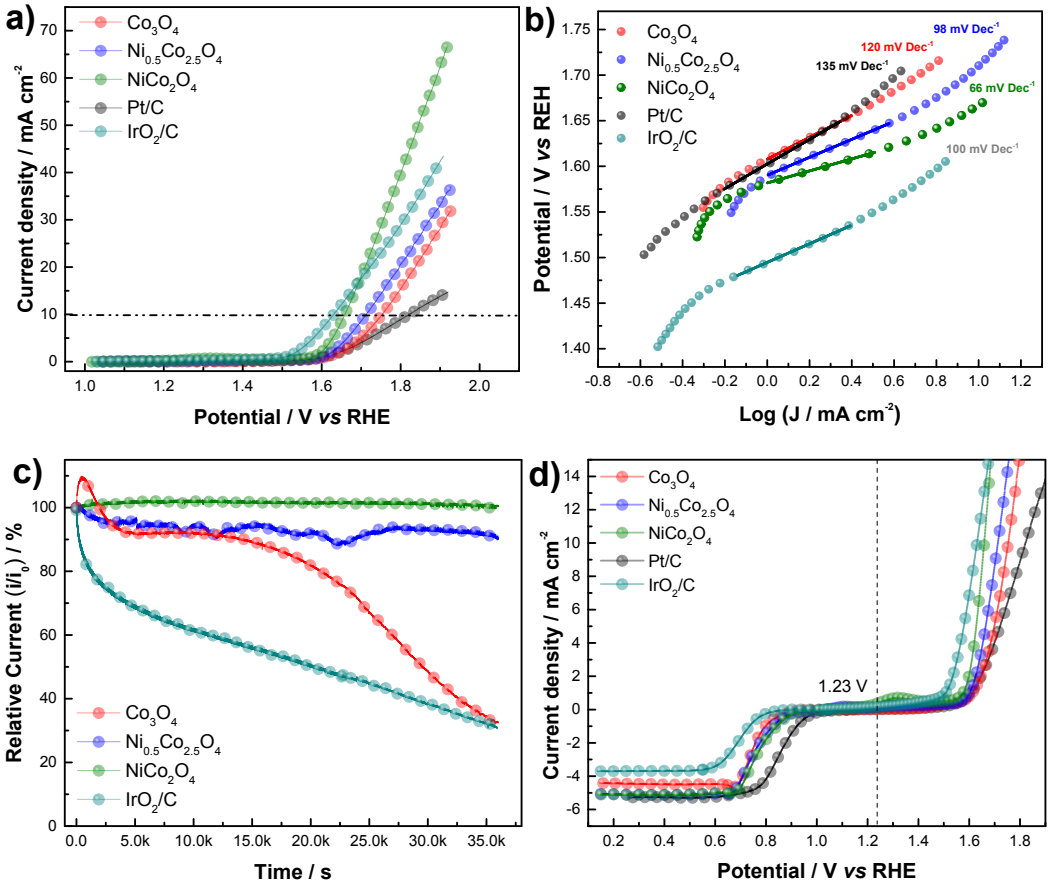

Figure 7. a) Electrocatalytic OER activity of the synthesized 3DOM spinels and their Pt/C and IrO_2 counter-parts. b) Tafel plots determined from the corresponding OER linear voltammetry. c) Chronoamperometric curves for OER stability in N_2-saturated 0.1 M KOH for the 3DOM spinels and IrO_2/C. d) Global polarization curves for the 3DOM spinels, Pt/C and IrO_2/C.

polarization losses are presented during the ORR and OER, and because of this, the ΔE determination is employed to evaluate the viability of materials to be used as bifunctional electrocatalysts. In this sense, ΔE can be calculated from the onset potential, or as other authors have suggested, from the difference between the potential to achieve 10 mA cm^{-2} during the OER and the half–wave potential during the ORR (Fig. 7d). A ΔE of 0.87 V was found for $NiCo_2O_4$, which was lower than that found for IrO_2/C (0.93 V) and Pt/C (0.97 V). Moreover, this potential difference was lower than that reported for many other highly active bifunctional materials (Table S5). In summary, the incorporation of Ni species into the Co_3O_4 spinel produced morphological changes, the BET surface area increased from 39.6 m^2 g^{-1} for Co_3O_4 to 46.8 m^2 g^{-1} for $NiCo_2O_4$ (20 % higher). Additionally, the Ni incorporation also resulted in electronic changes like the decrease of the resistance to charge transfer (R_{ct}) during ORR evaluation (Fig. S6). The R_{ct} decreased from 2743 (Co_3O_4) to 931 ($Ni_{0.5}Co_{2.5}O_4$) and then to 413 Ω cm^2 ($NiCo_2O_4$). This decrease can be attributed to the presence of Ni^{3+} which is known for its good electrical conductivity. The activity increase during OER can be related to the presence of Ni^{2+} species, which are known to be responsible of the improvement in other reported works, providing also electrochemical stability. The presence of these species was corroborated by XPS results (Fig. 5), where $NiCo_2O_4$ showed a higher content of Ni^{2+} and Ni^{3+} than $Ni_{0.5}Co_{2.5}O_4$. Thus, the improvement of activity and stability can be attributed to these aspects.

Zn–air battery evaluation. The excellent bifunctional behaviour of $NiCo_2O_4$ was the motivation to investigate its performance in a secondary Zn–air battery composed of 0.2 M $ZnCl_2$ + 4 M KOH electrolytic solution, a Zn foil anode and the bifunctional air electrode (Fig. 8a), 4M KOH was used because at this concentration the highest current density was obtained (Fig. S7). The discharge plot (Fig. 8b) indicated that open-circuit potentials of 1.44, 1.46 and 1.30 V were achieved by $NiCo_2O_4$, Pt/C and IrO_2/C, respectively. Pt/C displayed lower ohmic losses

than the other materials, achieving a higher current density. The lower activity of IrO_2/C to perform the ORR resulted in a decrement of the maximum current density compared with that value obtained when were used the other materials. In this way, the use of Pt/C resulted in a maximum power density of 109 mW cm^{-2}, while the use of $NiCo_2O_4$ produced 101 mW cm^{-2} , which was similar to the obtained by benchmarked Pt/C, and 24 mW cm^{-2} higher than that obtained by IrO_2/C. The charge–discharge plot (Fig. 8c) indicated that the $NiCo_2O_4$ 3DOM material possessed good reversibility at both low and high current densities. Considering 100 mA cm^{-2} as reference, $NiCo_2O_4$ exhibited 1.43 V of potential gap, while Pt/C presented a potential gap of 1.5 V. Similar tests were made for the mixture of benchmarked Pt/C + IrO_2/C displaying good reversibility (Fig. S8a). An accelerated charge–discharge test at 10 mA cm^{-2} (for both reactions) was undertaken to study the catalyst durability (Fig. 8d, and S8b). For both processes, $NiCo_2O_4$ displayed 2 V of initial charge potential and 1.2 V of discharge potential, whereas after 150 cycles (approximately 21 h), the charge potential increased to 2.1 V, while the discharge potential remained practically constant (1.14 V). In the cases of Pt/C only operated for 21 cycles, IrO_2/C operated for 130 cycles, and mixture operated for 21 cycles attributed to the negative effect of Pt/C (Fig. S8b). According to this data, the inability of Pt/C to perform the OER efficiently was attributed to low stability, while the need for more energy to achieve 10 mA cm^{-2} during the ORR was the cause of the stability loss in IrO_2/C. From these results, the round-trip energy efficiency was calculated for $NiCo_2O_4$, displaying at the first cycle 57.2 % of efficiency, and it decreased to 53.8 % at the final cycle.

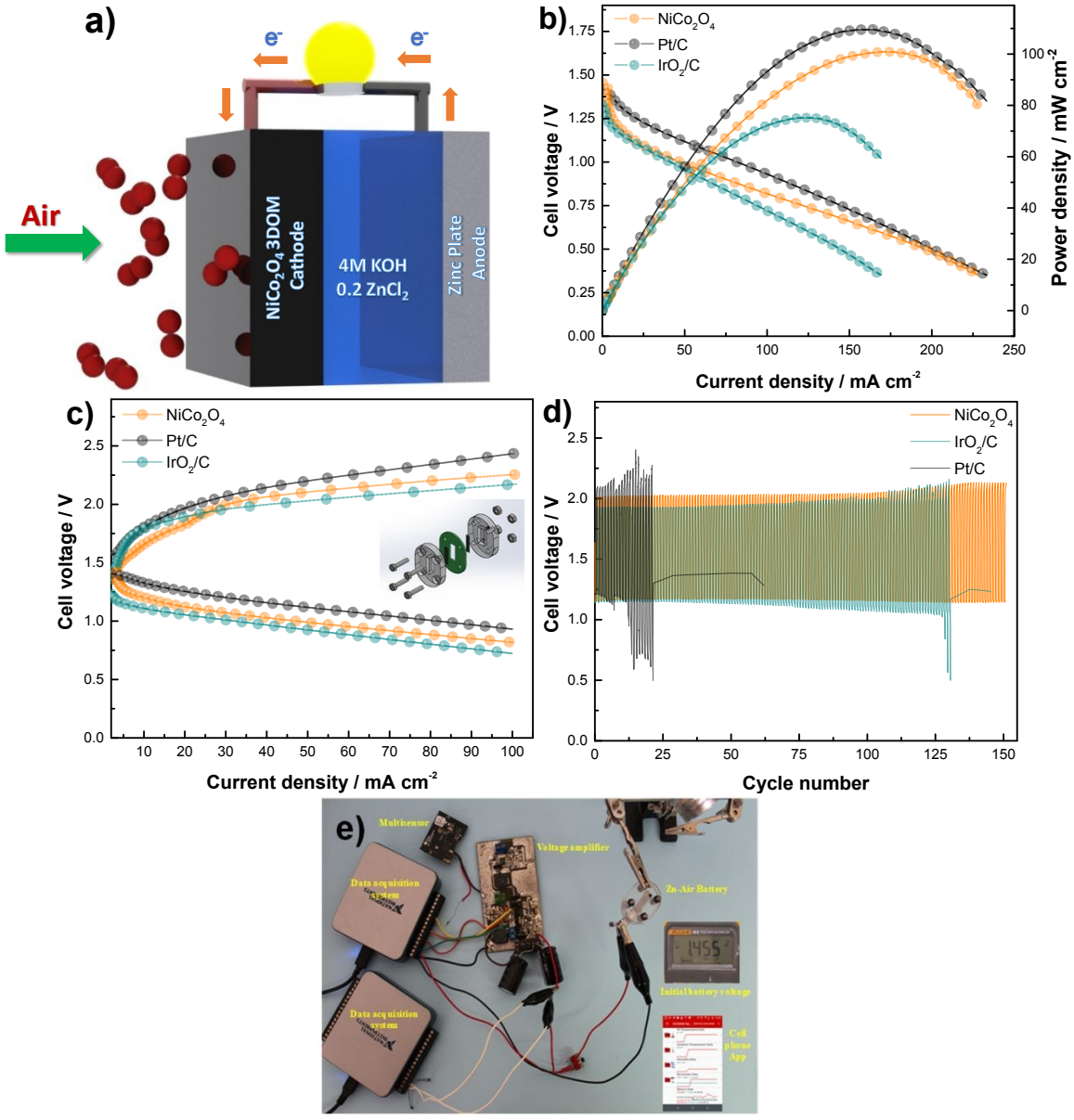

Figure 8. a) A schematic configuration of Zn-air battery. b) Polarization curves and their corresponding power densities for $NiCo_2O_4$, Pt/C and IrO_2/C. c) Charging and discharging polarization curves for the Zn-air battery using $NiCo_2O_4$, Pt/C and IrO_2/C cathodes. d) Charge and discharge cycling curves of rechargeable Zn-air battery based on $NiCo_2O_4$, Pt/C and IrO_2/ cathodes at 10 mA cm^{-2} with a duration of 500 seconds per cycle and e) System configuration used to power the multi-sensor using the Zn-Air battery.

View Article Online
DOI: 10.1039/D0TA00874E

ARTICLE

Finally, the capability of the $NiCo_2O_4$ 3DOM spinel to supply the energy requirements of a device was evaluated coupling this metal-air battery to a multi-sensor (Texas Instruments® model CC2650SensorTag, Fig. 8e). This device incorporates ten different low power sensors such as temperature, ambient light, gyroscope and humidity, which are accessible from an Android system (as cellphone) through the simplelink SensorTag® app. The battery was connected to the device multisensory through a homemade voltage amplifier (Fig. 8e), which increase the input voltage to an output voltage of 2.70 V. The initial voltage of the battery was 1.455V (Fig. 8e); when the device/Sensor is connected to the metal-air battery, the voltage decreased to 1.279 V due to energy demand of 10 mA of the sensor, finally the system was connected via Bluetooth to the cell phone, with a final voltage of 1.028 V. The system was operated continuously by 2 h with high stability of the battery showing 1.405 V of final voltage, like the initial value voltage. These results demonstrated that metal-air batteries based on 3DOM spinels electrocatalyst materials can be used in practical application with high performance and low cost.

Conclusions

This work demonstrated the feasibility to obtain different 3DOM spinels using a template of PMMA spheres with diameters close to 160 nm, which allowed to obtain surface areas from 39.6 $m^2\ g^{-1}$ for Co_3O_4 to 46.6 ± 0.2 $m^2\ g^{-1}$ for bimetallic $Ni_{0.5}Co_{2.5}O_4$ and $NiCo_2O_4$ 3DOM spinels. The increase in surface area displayed by the bimetallic spinels was attributed to the decrease in particle size from 11.9 nm to 8.6 / 9.6 nm. The multi–valences of the Co and Ni species in the $NiCo_2O_4$ 3DOM spinel and a higher Ni content than that in the $Ni_{0.5}Co_{2.5}O_4$ 3DOM spinel improved the activity towards the oxygen reduction / evolution reactions. $NiCo_2O_4$ 3DOM spinel presented a similar current density to that obtained when benchmarked Pt/C was used as catalyst in the ORR (5.11 vs. 5.25 mA cm^{-2}), and only displayed 80 mV of overpotential. According to the Tafel plots, this similarity in activities was related to the electrode kinetics, as both materials followed a 4 e^- pathway. Moreover, the improved activity of $NiCo_2O_4$ in comparison with that presented by the other 3DOM spinels was related to the presence and higher content of Ni providing high electrical conductivity to the material, enabling a decrease of the resistance to charge transfer from 2743 Ω cm^{-2} for Co_3O_4 to 413 Ω cm^{-2} for $NiCo_2O_4$ 3DOM spinel. In a similar way, the $NiCo_2O_4$ 3DOM spinel required only 10 mV more energy than a benchmarked IrO_2/C electrocatalyst to achieve 10 $mAcm^{-2}$ during the OER. Furthermore, the 3DOM spinel displayed a superior stability for both the ORR and OER, maintaining 80.5 % of initial current after 10 h of the ORR and 100 % during the OER. These differences in stabilities were related to the detachment of the catalytic ink instead of activity loss by deactivation of active sites. During the Zn–air battery tests, the $NiCo_2O_4$ 3DOM spinel enabled 1.44 V of open-circuit potential, which was like that obtained by using Pt/C (1.46 V). Moreover, because of its excellent activity as a bifunctional electrocatalyst, the $NiCo_2O_4$ 3DOM spinel displayed a superior charge–discharge capability after 21 h, while Pt/C operated only for 3 h. In summary, this work enlightens the possibility of using 3DOM structures in electrocatalysis, a field where this kind of material has not been used exhaustively, especially for the ORR and OER, and finally, confirms that 3DOM materials can be used in practical applications, such as Zn-Air batteries.

Conflicts of interest

There are no conflicts to declare.

Acknowledgements

The authors thank the Mexican Council for Science and Technology (CONACYT) for their financial support through projects CB-2015-01 Grant 256749, SENER 246079, Laboratorios Nacionales 2019-299058. Also, the authors acknowledge the TEM support provided by Cesar Cutberto Leyva Porras from CIMAV-Nanotech.

Notes and references

1 H.-F. Wang and Q. Xu, *Matter*, 2019, **1**, 565–595.
2 H. F. Wang, C. Tang and Q. Zhang, *Adv. Funct. Mater.*, 2018, **28**, 1–22.
3 and Z. C. Jing Fu, Zachary Paul Cano, Moon Gyu Park, Aiping Yu, Michael Fowler, *Adv. Mater.*, 2017, **29**, 1–34.
4 J. Pan, Y. Y. Xu, H. Yang, Z. Dong, H. Liu and B. Y. Xia, *Adv. Sci.*, 2018, **5**, 1–30.
5 M. Xu, D. G. Ivey, Z. Xie and W. Qu, *J. Power Sources*, 2015, **283**, 358–371.
6 J. S. Lee, S. T. Kim, R. Cao, N. S. Choi, M. Liu, K. T. Lee and J. Cho, *Adv. Energy Mater.*, 2011, **1**, 34–50.
7 X. Cai, L. Lai, J. Lin and Z. Shen, *Mater. Horizons*, 2017, **4**, 945–976.
8 V. Caramia and B. Bozzini, *Mater. Renew. Sustain. Energy*, 2014, **3**, 1–12.
9 C. Roth, N. Benker, R. Theissmann, R. J. Nichols and D. J. Schiffrin, *Langmuir*, 2008, **24**, 2191–2199.
10 L. Yuan, Z. Yan, L. Jiang, E. Wang, S. Wang and G. Sun, *J. Energy Chem.*, 2016, **25**, 805–810.
11 S. Ghosh, P. Kar, N. Bhandary, S. Basu, S. Sardar, T.

Maiyalagan, D. Majumdar, S. K. Bhattacharya, A. Bhaumik, P. Lemmens and S. K. Pal, *Catal. Sci. Technol.*, 2016, **6**, 1417–1429.
12 J. Il Jung, H. Y. Jeong, J. S. Lee, M. G. Kim and J. Cho, *Angew. Chemie - Int. Ed.*, 2014, **53**, 4582–4586.
13 T. Maiyalagan, K. A. Jarvis, S. Therese, P. J. Ferreira and A. Manthiram, *Nat. Commun.*, 2014, **5**, 1–8.
14 A. Pendashteh, J. Palma, M. Anderson and R. Marcilla, *Appl. Catal. B Environ.*, 2017, **201**, 241–252.
15 J. C. Li, P. X. Hou, S. Y. Zhao, C. Liu, D. M. Tang, M. Cheng, F. Zhang and H. M. Cheng, *Energy Environ. Sci.*, 2016, **9**, 3079–3084.
16 J. Zhang, Z. Zhao, Z. Xia and L. Dai, *Nat. Nanotechnol.*, 2015, **10**, 444–452.
17 L. Wang, F. Yin and C. Yao, *Int. J. Hydrogen Energy*, 2014, **39**, 15913–15919.
18 H. Osgood, S. V. Devaguptapu, H. Xu, J. Cho and G. Wu, *Nano Today*, 2016, **11**, 601–625.
19 Q. Zhao, Z. Yan, C. Chen and J. Chen, *Chem. Rev.*, 2017, **117**, 10121–10211.
20 B. M. Hunter, H. B. Gray and A. M. Mu, *Chem. Rev.*, 2016, **116**, 14120–14136.
21 H. S. Jeon, M. S. Jee, H. Kim, S. J. Ahn, Y. J. Hwang, B. K. Min and J. Accepted, *Appl. Mater. Interfaces*, 2015, **7**, 24550–24555.
22 J. Zeng, C. Francia, J. Amici, S. Bodoardo and N. Penazzi, *J. Power Sources*, 2014, **272**, 1003–1009.
23 A. N. and R. D. R. M. Fayette, *J. Mater. Chem.*, 2015, **3**, 4274–4283.
24 R. Gao, J. Zhu, X. Xiao, Z. Hu, J. Liu and X. Liu, *J. Phys. Chem. C*, 2015, **119**, 4516–4523.
25 F. Zhang, L. Wang, P. Xiao, K. Yuan, M. Lai and J. M. C. A, *J. Mater. Chem. A*, 2016, **4**, 6350–6356.
26 C. X. K. and B. E. K. Zhu Chen, *Phys. Chem. Chem. Phys.*, 2015, **17**, 29387–29393.
27 R. Chen, H. Wang, J. Miao, H. Yang and B. Liu, *Nano Energy*, 2015, **11**, 333–340.
28 Z. Y. and R. Y. Chao Jin, Fanliang Lu, Xuecheng Cao, *J. Mater. Chem. A*, 2013, **1**, 12170–12177.
29 B. Y. Li, P. Hasin and Y. Wu, *Adv. Mater.*, 2010, **22**, 1926–1929.
30 H. Shi and G. Zhao, *J. Phys. Chem. C*, 2014, **118**, 25939–25946.
31 H. Xue, S. Wu, J. Tang, H. Gong, P. He, J. He and H. Zhou, *Appl. Mater. Interfaces*, 2016, **8**, 8427–8435.
32 X. Li, J. Iocozzia, Y. Chen, S. Zhao, X. Cui, W. Wang, H. Yu, S. Lin and Z. Lin, *Angew. Chemie - Int. Ed.*, 2018, **57**, 2046–2070.
33 A. Stein, B. E. Wilson, S. G. Rudisill and A. Stein, *Chem Soc Rev*, 2013, **42**, 2763–2803.
34 J. H. and A. Stein, in *Handbook of Solid State Chemistry*, 2017, pp. 243–274.
35 Y. Wei, Z. Zhao, J. Jiao, J. Liu, A. Duan and G. Jiang, *Catal. Today*, 2015, **245**, 37–45.
36 B. Jin, Y. Wei, Z. Zhao, J. Liu, Y. Li, R. Li and A. Duan, *Chinese J. Catal.*, 2017, **38**, 1629–1641.
37 N. Feng, Y. Wu, J. Meng, C. Chen, L. Wang and H. Wan, *RSC Adv.*, 2015, **5**, 91609–91618.
38 S. H. Wan and G. Guan, *Catal. Sci. Technol.*, 2016, **6**, 7718–7728.
39 X. Yu, Z. Zhao, Y. Wei and J. Liu, *Sci. Rep.*, 2017, **7**, 1–19.
40 H. Lin, P. liu, S. Wang, Z. Zhang, Z. Dai, S. Tan and D. Chen, *J. Power Sources*, 2019, **412**, 701–709.
41 M. G. Park, D. U. Lee, M. H. Seo, Z. P. Cano and Z. Chen, *Small*, 2016, **12**, 2707–2714.
42 W. N. and F. M. D Distler, *Encycl. Mater. Sci. Technol. (Second Ed.*, 2017, 1–14.
43 W. D. Harkins, *J. Am. Chem. Soc.*, 1947, **69**, 1428–1444.
44 Y. Wei, Z. Zhao, T. Li, J. Liu, A. Duan and G. Jiang, *Appl. Catal. B Environ.*, 2014, **146**, 57–70.
45 C. A. Schneider, W. S. Rasband and K. W. Eliceiri, *Nat. Methods*, 2012, **9**, 671.
46 P. E. Sobol and J. Chastain, *Handbook of X-ray Photoelectron Spectroscopy: A Reference Book of Standard Spectra for Identification and Interpretation of XPS Data*, Physical Electronics Division, Perkin-Elmer Corporation, Eden Prairie Minnesota, Ilustrada., 1992.
47 Y. Zhou, Y. Liu, W. Zhao, H. Wang, B. Li, X. Zhou and H. Shen, *Sci. Rep.*, 2015, **5**, 11584–11595.
48 M. Kazazi and R. Karami, *Solid state Ionics*, 2017, **308**, 8–15.
49 Z. A. Alothman, *Materials (Basel).*, 2012, **5**, 2874–2902.
50 F.-Z. M. and X.-B. Z. Ji-Jing Xu, Zhong-Li Wang, Dan Xu, *Energy Environ. Sci.*, 2014, **7**, 2213–2219.
51 J. Xu, J. Liu, Z. Zhao, J. Zheng, G. Zhang, A. Duan and G. Jiang, *Catal. Today*, 2010, **153**, 136–142.
52 J. Xu, J. Liu, Z. Zhao, C. Xu, J. Zheng, A. Duan and G. Jiang, *J. Catal.*, 2011, **282**, 1–12.
53 J. H. Zhong, A. L. Wang, G. R. Li, J. W. Wang, Y. N. Ou and Y. X. Tong, *J. Mater. Chem.*, 2012, **22**, 5656–5665.
54 O. Nico, M. Gracia, L. Gautier, H. M. Palmer and F. J. Berry, *J. Mater. Chem.*, 2001, **11**, 3087–3093.
55 J. F. Marco, J. R. Gancedo, J. Ortiz and J. L. Gautier, *Appl. Surf. Sci.*, 2004, **227**, 175–186.
56 P. C. J. L. G. E. Ríos, H. Nguyen-Cong, J.F. Marco, J.R. Gancedo, *Electrochim. Acta*, 2000, **45**, 4431–4440.
57 S. Li, J. Du and J. Zhang, *Microchim Acta*, 2014, **181**, 631–638.
58 A. Salimi, H. Mamkhezri, R. Hallaj and S. Soltanian, *Sensors Actuators, B Chem.*, 2008, **129**, 246–254.
59 J. Wang, T. Qiu, X. Chen, Y. Lu and W. Yang, *J. Power Sources*, 2014, **268**, 341–348.
60 V. Gupta, S. Gupta and N. Miura, *J. Power Sources*, 2010, **195**, 3757–3760.
61 E. B. Castro and C. A. Gervasi, *Int. J. Hydrogen Energy*, 2000, **25**, 1163–1170.
62 H. Wang, S. Hung, H. Chen, T. Chan, H. M. Chen and B. Liu, 2016, **4**, 8–11.
63 M. Lyons and M. Brandon, *Int. J. Electrochem. Sci.*, 2008, **3**, 1425–1462.
64 M. E. G. Lyons and M. P. Brandon, *Int. J. Electrochem. Sci.*, 2008, **3**, 1386–1424.

View Article Online
DOI: 10.1039/D0TA00874E

Table of Contents Entry

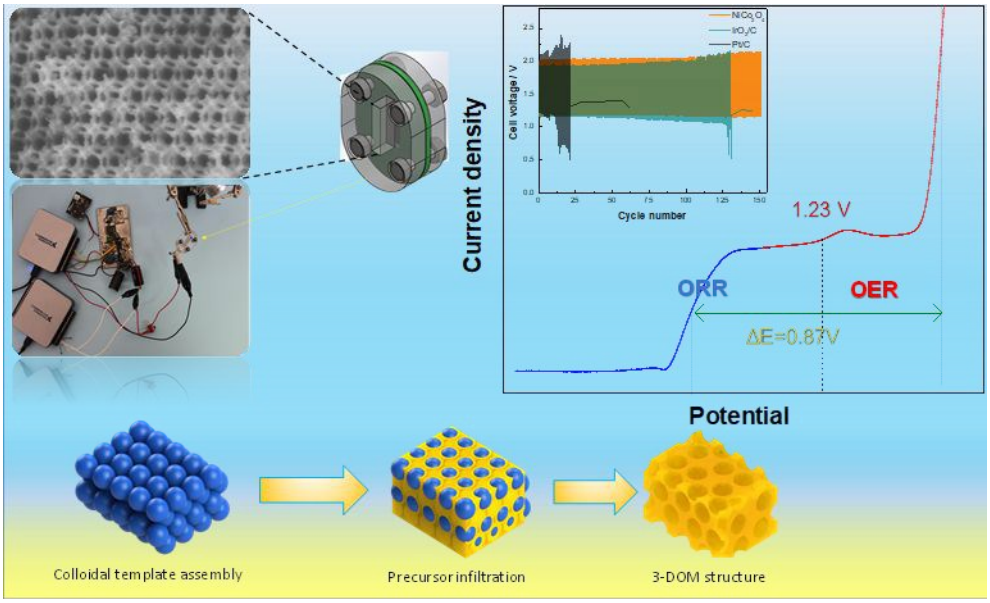

A rechargeable Zn-air battery was assembled using $NiCo_2O_4$ three-dimensionally ordered macroporous (3DOM) spinel displaying an open circuit potential of 1.44 V, a power density of 101 mW cm^{-2}, and a high durability during charge/discharge cycling curves (being operated for 21 h). In addition, the resulting device can supply the energy demand of a remote multi-sensor.